Localization of the dopant in Ge:Mn diluted magnetic semiconductors by x-ray absorption at the Mn K edge

2010 J. Phys.: Condens. Matter 22 216006

(http://iopscience.iop.org/0953-8984/22/21/216006)

J. Phys.: Condens. Matter **22** (2010) 216006 (10pp) doi:10.1088/0953-8984/22/21/216006

Localization of the dopant in Ge:Mn diluted magnetic semiconductors by x-ray absorption at the Mn K edge

R Gunnella[1], L Morresi[1], N Pinto[1], A Di Cicco[1], L Ottaviano[2], M Passacantando[2], A Verna[2], G Impellizzeri[3], A Irrera[3] and F d'Acapito[4]

[1] CNISM-Dipartimento di Fisica, Università di Camerino, Via Madonna delle Carceri, I-62032 Camerino (MC), Italy
[2] Dipartimento di Fisica, Università dell'Aquila, Via Vetoio, I-67010, Coppito (AQ), Italy
[3] MATIS-INFM and Dipartimento di Fisica e Astronomia, Università di Catania, I-95123 Catania, Italy
[4] CNR-INFM-OGG, c/o ESRF 6, Rue Jules Horowitz, F-38043 Grenoble, France

Received 19 February 2010, in final form 11 April 2010
Published 5 May 2010
Online at stacks.iop.org/JPhysCM/22/216006

Abstract
A unitary picture of the structural properties of Mn_xGe_{1-x} diluted alloys fabricated by either ion implantation or molecular beam epitaxy (MBE), at various growth temperatures (from 80 to about 623 K) and few per cent concentrations, is proposed. Analysis is based on synchrotron radiation x-ray absorption spectroscopy at the Mn K edge. When the growth temperature exceeds 330 K, the MBE samples show a high number of precipitated ferromagnetic nanoparticles, mainly Mn_5Ge_3, nucleated from the previous occupation of interstitial tetrahedral sites. Efficient substitution is observed in the case of MBE samples made by alternate layers of GeMn alloys grown at $T \leqslant 433$ K and undoped Ge thick layers. Similar good dilution properties are obtained by implanting Mn ions at low temperatures (80 K). Possible precursors to preferential mechanisms in the alloy formation are discussed on the basis of the present comparative study.

(Some figures in this article are in colour only in the electronic version)

1. Introduction

The achievement of ferromagnetism (FM) in Ge by simple introduction of a magnetic transition metal (TM) atom (Mn, Cr, Fe) attracted considerable attention due to the expected full compatibility with the mainstream silicon technology [1]. Hopefully, such an approach will allow us to finely control polarized currents and will assure both semiconductivity or half-metallicity and magnetic ordering [2].

However, due to the very low solubility limit of Mn in Ge (10^{15} cm^{-3}) [3], corresponding to an atomic per cent of about 0.2×10^{-6}, i.e. several orders of magnitude below the typical Mn concentration employed in the fabrication of MnGe alloys, growth of homogeneous phases of diluted alloys is challenging. The magnetic response of most of the Mn_xGe_{1-x} alloys fabricated so far is then probably due to Mn-rich separated phases. In only a few cases, proof of a diluted magnetic semiconductor (DMS), i.e. an efficient and homogeneous dilution of magnetic acceptor impurities in the semiconducting matrix, has been obtained [1, 4–7].

Formation of both metal-rich precipitates and the unintentional donor-like doping by occupation of interstitial sites [8], represent two main limitations to overcome in the fabrication of a successful DMS. To limit the importance of the above processes and at the same time to improve the solubility of the metal impurities in the matrix one can reduce the TM concentration even further to about 1% [9, 10]. However, if the main task is to increment the number of magnetically active atoms, two paths can be pursued: (1) reduction of the growth temperature, possibly followed by post-growth treatment; (2) introduction of energy barriers against undesired reaction paths.

One interesting way to improve Mn dilution in semiconductors is the growth of δ doped layers of Mn [7],

i.e. a non-equilibrium growth of a fraction of monolayer of Mn alternated with a semiconductor layer. This method is used to fabricate digital layer (DL) alloy heterostructures, when alloys with a high TM concentration are alternated with undoped SC layers. In such DL heterostructures, a sizable increase in the Curie temperature (T_C) has been measured due to the reduction of interstitial site occupation during the growth of III–V DMS alloys at low temperatures [11].

Another technique which is supposed to raise substantially the solubility limit and avoid the precipitation of intermetallic alloys is ion implantation, which in the case of the Ge DMSs has been investigated initially by Liu *et al* [12] and more extensively in more recent works [13–17]. From these studies the coexistence of different phases of alloy with intermetallic character, surrounded by extended regions with Mn dilution, was detected for implantation temperatures above 450 K. The possibility to reduce intermetallic formation by lowering the implantation temperature was also investigated. In particular, it is worth studying the implantation at RT or below RT.

In fact, for implantation temperatures ranging from RT to 450 K [17, 18], an onset of strong swelling and amorphization of the film with transformation to a spongelike structure was observed.

In spite of several investigations assessing the presence of precipitated phases in DMSs, or, in general, of defects in addition to the substitutional incorporation of magnetic impurities, not many techniques provide quantitative determination of the relative abundances of such phases. This is especially true in case of low Mn concentrations with substoichiometry of the alloyed components giving rise to a strongly reduced contrast in transmission electron microscopy (TEM) images. At higher dopant concentrations, TEM images of implanted samples showed a sizable reduction of defects (precipitates) with respect to MBE samples [15], while at low temperature (close to RT) the films turned out to be amorphous. In particular the amorphous regions turned to polycrystalline after annealing in vacuum (400 °C) [17].

From the magnetic characteristics point of view and their close relationship with the structural properties, multiple phases are often measured in MnGe alloys. The presence of the Mn_5Ge_3 precipitates with a 'hard' magnetic component with T_C up to 270 K and relevant coercivity (600 Oe at 150 K) dominates over the softer component attributed to the diluted phase with lower coercivity, remanence and T_C well below RT [16]. By controlling the precipitation, the soft component can exceed RT as in the case of implantation at LN temperature [19].

There is no doubt that only the use of probes with chemical sensitivity, like x-ray absorption spectroscopy (XAS), can safely reveal the structure of Mn diluted in the matrix [16]. XAS studies at the near edge region (XANES) or at the extended energy range (EXAFS) of the Mn K edge resulted in a profitable technique to obtain information complementary to TEM or x-ray diffraction (XRD) investigations. Only a few works were devoted to XAS applications to III–V [20, 21] and to IV–IV DMSs [15, 22, 23]. EXAFS directly provides with high precision the nearest neighbor distances and coordination numbers surrounding the TM atom by the study of the scattering of the photoemitted electrons. On the other side XANES sensitivity to the coordination geometry and bond lengths can be fully exploited, though a time consuming trial and error approach is required.

The aim of the present work was to investigate the structural problem of Ge:Mn DMSs in order to highlight the formation and the evolution of the alloys prepared by means of different growth techniques. In particular we focused on (1) the conditions to develop homogeneous dilution, (2) the structural problem during the non-equilibrium alloy formation, (3) the role of defects, oxidation and morphology in the film structure, (4) the dilution in the amorphous phase followed by post-growth annealing.

The outline of the present work includes in section 2 a description of the experiment. In section 3 the XANES region is analyzed. In section 4 the details of the EXAFS fitting are reported, while the conclusions of the work follow in section 5.

2. Experimental details

Two kinds of samples were prepared: (a) by means of ion implantation at fixed beam energy, producing implanted films with varying concentration profiles; (b) by means of MBE at several temperatures and concentrations.

In the former case, chemically cleaned intrinsic Ge(100) single crystal wafers were implanted with 100 keV Mn^+ ions with a fluence of 2×10^{16} at cm^{-2}, and substrate temperatures ranging between 80 and 513 K. Samples were optionally annealed for 1 h in ultrahigh vacuum at 673 K to avoid amorphization (as in [24]). Samples showing oxidized surfaces were sputtered by Ar^+ ions, with 2 keV energy at an incidence angle of 45° with respect to the sample normal. The average and peak value of the Mn content were 4% and 9% respectively. The concentration peak was located at 50 nm below the surface while the projected range turned out to be 130 nm. Previous studies of implanted samples at growth temperature of 613 K showed almost complete dilution in the subsurface layer [15], while deeper regions of the film showed the presence of precipitated clusters. In the room temperature (RT) implanted samples, a porous film due to the amorphization and swelling of the Mn–Ge layer [17] was observed. An amorphous Ge layer containing Mn below the porous layer was converted to polycrystalline upon annealing at 673 K [17]. Implantation below RT was not affected by swelling and the amorphous layer showed a marked contrast with respect the Ge crystalline substrate, while the surface was good and mirror-like on visual inspection. Furthermore, annealing processes did not modify such a structure, indicating a remarkable stability of the implanted films.

GeMn films (average thickness 40 nm) were also grown by MBE coevaporation on epi-ready n-type Ge(001) wafers with a nominal resistivity of 2.5–7.5 Ω cm [9, 25, 26]. The substrate preparation consisted in thermal desorption of the oxide at a temperature of about 670 K for 30 min, soon after followed by the growth of one 150 nm thick Ge buffer layer at 620 K. Film growth was carried out at several substrate temperatures, ranging from 343 to 620 K. A number of characterization

techniques have recently been used to investigate the film properties [10, 13–17, 25–27].

Moreover, we report our investigations of DL alloy samples $(Mn_{0.3}Ge_9)_{30}$ with a nominal 3% Mn concentration, consisting of 30 periods of 0.3 ML of Mn and 9 ML of Ge (1 ML = 1.42 Å) for a total thickness of 40 nm.

Finally, a solid phase epitaxy (SPE) Mn_5Ge_3 alloy deposited on a Ge(111) substrate with a nominal resistivity of 0.38–0.46 Ω cm was used as a reference together with other commercial high purity compounds for metallic Mn, MnO, and Mn_2O_3 standards [27].

The EXAFS measurements were carried out at the Mn K edge (6539 eV) on the GILDA-CRG beamline at the European Synchrotron Radiation Facility [28]. The monochromator was equipped with a pair of Si(311) crystals (estimated bandwidth 1/10 000) and was run in dynamic focusing mode [29]. The harmonic rejection was achieved by using a pair of Pd-coated mirrors working in grazing incidence with a cutoff energy of 18 keV. The incoming beam was read by a N_2 filled ion chamber, whereas the Mn Kα fluorescence signal was detected by a 13 element high purity Ge detector.

All the EXAFS measurements were performed at room temperature if not otherwise specified and a metal reference sample was used to calibrate the photon beam energy during the measurement sessions.

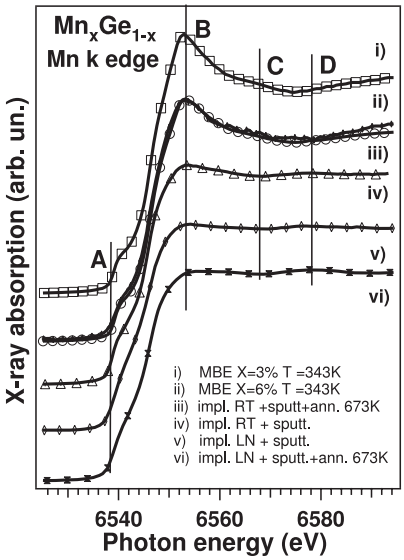

Figure 1. Mn K-edge XANES of MBE films grown at 343 K at 3% (i) and 6% (ii) concentration compared with RT implanted samples after sputtering without annealing (iii) or sputtering and annealing at 673 K (iv). Spectrum (v) reports the case of an LN implanted sample and (vi) the same sample after annealing at 673 K. Continuous lines represent guides for the eye.

3. Near edge analysis (XANES)

XANES analysis is extremely sensitive to parameters like nearest neighbor distances, but in addition to EXAFS a more direct relationship with coordination geometry could be established by a trial and error procedure involving *ab initio* calculation methods. Nevertheless, here our aim was to correlate the spectral signatures through the whole set of Ge DMS samples to establish mutual correlations between samples grown in different conditions and by different growth techniques.

In figure 1 we found a first relationship between MBE and ion implanted samples grown at low temperatures. Spectra of MBE samples grown at 343 K (spectra (i) and (ii) at 3% and 6% Mn concentrations respectively) were reported along with samples grown by implantation at room temperature (RT) (spectra (iii) and (iv)), at liquid nitrogen (LN) temperature (spectrum (v)) and at LN temperature with post-growth annealing at 673 K (spectrum (vi)). Growth or incorporation at low temperatures resulted in well aligned features in all cases. In particular a similarity was observed for samples (ii) and (iii), prepared by RT ion implantation (followed by sputtering and annealing at 673 K) and by MBE ($T = 343$ K), respectively.

The spectra were constituted by four main peaks (from A to D): the pre-peak A (6540 eV) was difficult to assess as it could be either assigned to forbidden transitions or to the presence of Mn metallic particles inside the film. The white line (peak B) at 6553 eV was strongly affected by the Mn concentration as might be evident by looking at spectrum (i) and spectrum (ii) of MBE samples grown at 343 K when such a concentration was increased from 3 to 6%. The latter spectrum (ii) was completely superposed on spectrum (iii) of implanted Mn at RT after sputtering and annealing at 673 K. The RT implanted sample sputtered without annealing (spectrum (iv)) showed a reduction of the white line and the presence of a peak labeled D (6579 eV) not present in the sputtered and annealed samples of spectrum (iii). A corresponding absence of peak C (6567 eV) in spectra (iii) and (iv) was also observed. In figure 1 the XANES spectra of the LN temperature implanted samples (spectrum (v)) and the spectra of the same samples after annealing at 673 K (spectrum (vi)) were reported. In contrast to the implanted samples at RT, the remarkable stability with respect to high temperature annealing of LN implanted samples was immediately evident.

In figure 2, spectra of samples grown at temperatures higher than 433 K, from ion implantation (spectrum (i)) and MBE (spectra from (ii) to (iv)), were reported. The Mn_5Ge_3 alloy spectrum (v) is also reported for direct comparison. The fingerprints of the Mn-rich alloy precipitated clusters, two characteristic features at 6563 eV (B) and 6575 eV (C), followed by a deep minimum at 6586 eV (D), were present in all the samples grown by MBE at temperatures of 523 K (spectrum (ii)) or higher (not shown), but with less evidence also in the MBE sample grown at 433 K (spectra (iii)). A few of the Mn-rich inclusions were visible in the implanted sample at 543 K subsequently annealed at 673 K (spectrum (i)) and in the DL alloy grown at 433 K (spectrum (iv)). In particular for the DL samples, indication of a different behavior with respect to the other spectra was the presence of a peak at 6579 eV (E) and the lack of the deep minimum at 6586 eV (D).

By direct comparison of intensity and position of the main features of the reference spectra, straightforward information concerning the metallic character or the occurrence of oxidation in the films could be obtained.

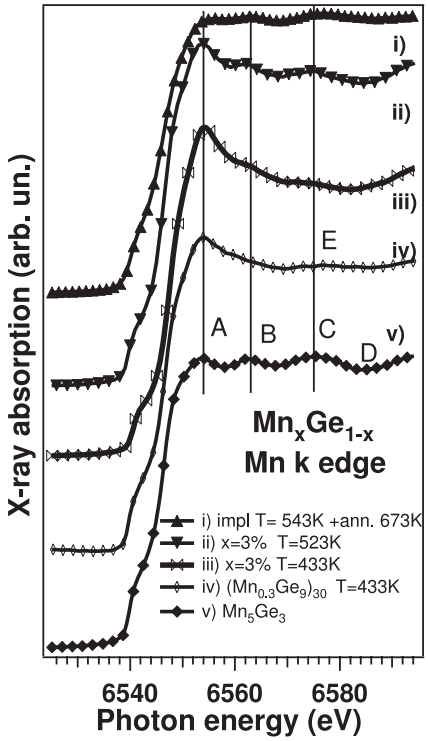

Figure 2. Mn K-edge XANES of implanted samples grown at $T = 543$ K and annealed at 673 K (i) compared with MBE samples grown at 523 K (ii) and MBE samples grown at $T = 433$ K at 3% (iii) concentration, and finally the DL sample grown at $T = 433$ K (iv). As a reference, the SPE sample of Mn_5Ge_3 (v) is reported. Continuous lines represent guides for the eye.

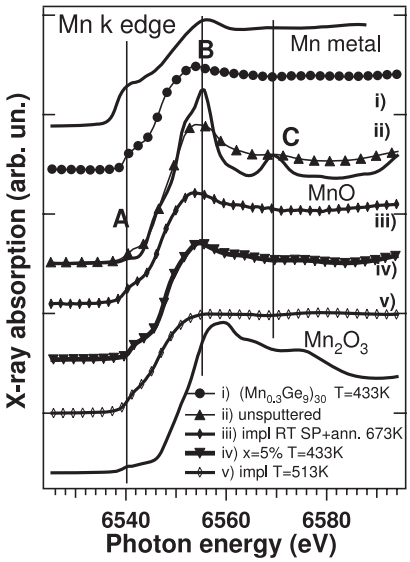

Figure 3. Mn K-edge XANES of several samples discussed above (symbols) compared with standard references for Mn oxides and metallic Mn (continuous lines as guide for the eyes).

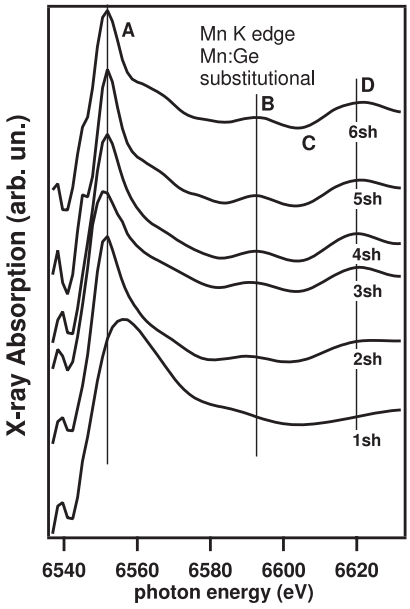

Figure 4. Shell by shell multiple scattering calculations of the Mn K edge in Mn:Ge alloys within a purely substitutional site occupation model.

For instance, we carefully checked contamination of the samples due to the oxidation of Mn. A sizable number of defects, like pin-holes, roughness and mosaicity, might enhance oxygen migration in the sample when the substrate is kept at low temperatures during the growth. In figure 3 are reported, by continuous lines, spectra of reference samples, i.e. from top to bottom metallic Mn, MnO and Mn_2O_3 respectively.

It turned out to be quite evident that oxidation did not appreciably affect the deeper layers of samples we analyzed, confirming that Mn oxidation proceeded slowly inside a Ge crystal, in substantial agreement with a recent XAS Mn $L_{2,3}$ analysis [30].

In particular, the lack of oxygen contamination in the Mn diluted samples was proved by the absence of the peak labeled C at 6569 eV (figure 3) of the MnO spectra.

However, one notable exception in figure 3 was spectrum (ii), which represented the case of the as-grown implanted sample at RT without sputtering. The position and intensity of the spectrum features clearly pointed to a sizable presence of MnO.

Spectrum (iii) of figure 3 represents the same sample as spectrum (ii) after sputtering and annealing at 673 K. The recovery of the positions and intensities of the peaks of the oxide free alloy was clear.

Additional information on the MnGe alloy structure could be obtained by means of multiple scattering calculations of the XAS spectra of selected models to be compared to the experimental spectra.

Calculations were performed by means of a muffin-tin multiple scattering approach, recently reviewed in [31]. Such calculations are based on a suitable choice of a spherical cluster surrounding the absorbing atom and proper convolution due to experimental and lifetime broadening amounting to 0.7 eV. Little influence of the Mn concentration on the XAS calculations was verified for values ranging between 6 and 25%. The calculations were performed for the substitutional (S), interstitial tetrahedral (T) and hexagonal (H) site occupation of the dopant Mn and are reported in figure 4 and in figure 5 respectively.

Table 1. Mn nearest neighbor (NN) and next NN distances from the Mn absorbing atom for the three models of substitutional (S), interstitial tetrahedral (T) and interstitial hexagonal (H) Mn in Ge.

Site occupation	(N1, $\Re$1)	(N2, $\Re$2)	(N3, $\Re$3)	(N4, $\Re$4)	(N5, $\Re$5)	(N6, $\Re$6)
Substitutional (S)	(4, 2.44)	(12, 3.99)	(12, 4.68)	(6, 5.66)	(12, 6.16)	(24, 6.91)
Int. hexagonal (H)	(6, 2.34)	(8, 3.66)	(6, 4.63)	(9, 5.42)	(13, 6.11)	(6, 6.72)
Int. tetrahedral (T)	(4, 2.44)	(6, 2.82)	(12, 4.68)	(8, 4.89)	(12, 6.16)	(24, 6.31)

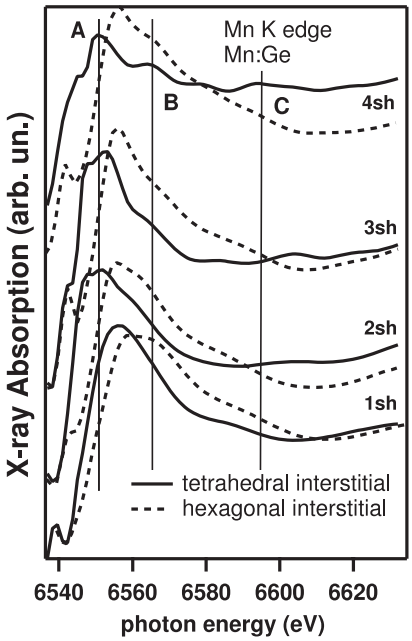

Figure 5. Shell by shell multiple scattering calculations of the Mn K edge in Mn:Ge alloys according to an interstitial T (continuous line) or H (dashed line) occupation site model.

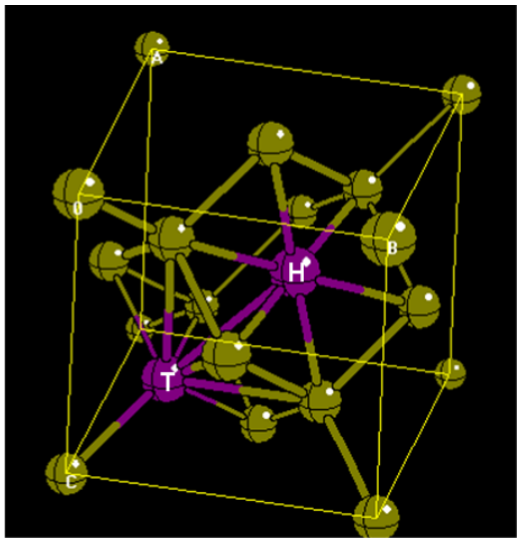

Figure 6. Stick and ball model of interstitial T and H occupation sites within the Ge unit cell. The *c* axis is pointing towards the bottom.

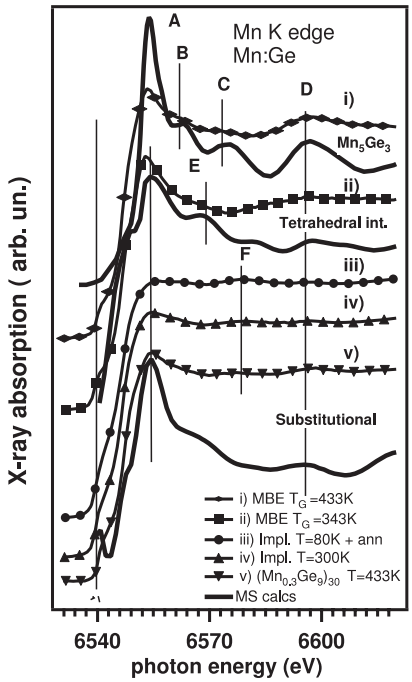

Figure 7. Comparison of Mn K edge of selected samples (from (i) to (v)) compared with calculations of models related to the following systems: MnGe alloy, interstitial T and substitutional Mn.

In these figures the shell by shell contributions were singled out according to the structural parameters reported in table 1. In figure 5 both the XANES for an absorbing Mn at the tetrahedral interstitial (T) site at the (1/4, 1/4, 3/4) position and at the hexagonal interstitial (H) site at the (3/8, 5/8, 3/8) position of the cubic cell (see the stick and ball model in figure 6) were reported.

In figure 7 we have plotted by symbols experimental data for spectra from (i) to (v) and by continuous lines the theoretical XAS spectra which we consider the most representative ones. The calculations include the Mn_5Ge_3 alloy, the tetrahedral interstitial (T) and the substitutional (S) occupation sites according to the shell parameters reported in table 2.

As can be seen from figure 7, the Mn_5Ge_3 alloys showed spectral features at well defined energies: 6553 (A), 6563 (B), 6575 (C) and 6596 (D) eV. In the tetrahedral interstitial site case, intensity maxima at 6566 (E) and at 6596 (D) eV were found. MBE samples grown at low temperatures or samples implanted at low temperatures showed the main features at 6579 (F) and 6596 (D) eV. An almost structureless XAS calculation was obtained for the H site and is not reported in this comparison. In this regard, *ab initio* calculations indicating that the H interstitial site was by far the unfavored one when compared to the T or the S site [32] supported such a choice. However, it ought to be considered that a high degree of strain was expected around the H site because of the short Mn–Ge distance (2.35 Å) and could eventually affect these conclusions.

Table 2. Mn NN and next NN distances for the two non-equivalent prototypical Mn absorbing atoms in the Mn_5Ge_3 alloy: Mn1 and Mn2 of relative population 40% and 60%, respectively.

Mn type	(N1, $\Re$1)	(N2, $\Re$2)	(N3, $\Re$3)	(N4, $\Re$4)	(N5, $\Re$5)
Mn1	(Mn(2), 2.53)	(Ge(6), 2.54)	(Mn(6), 3.06)	(Mn(3), 4.14)	(Ge(3), 4.38)
Mn2	(Ge(2), 2.4)	(Ge(1), 2.6)	(Ge(2), 2.77)	(Mn(10), 3.02)	(Mn(2), 4.27)

From the comparison of calculations with spectrum (i) of figure 7, we drew the conclusion that samples grown at 433 K or higher temperatures all underwent a transition to an intermetallic compound as shown by the excellent agreement with the Mn_5Ge_3 alloy. In a similar manner to what was found for the III–V DMS [33], the low temperature MBE grown MnGe samples ($T = 343$ K) (figure 7 spectrum (ii)) showed a particular difference from the samples grown at 433 K at the same concentration of $x = 3\%$ (spectrum (i)). For instance, similarities with the theoretical calculations of Mn occupation in the interstitial T site in figure 7 were visible. In particular, the resonance at 6566 eV (E) is a quite particular fingerprint of the absorption for this latter occupation site.

Within the sensitivity of this qualitative analysis, a rather good agreement between the pure substitutional model in figure 7 and the three spectra grown at lower temperatures, namely, the LN implanted samples (spectrum (iii)), the after sputtering RT implanted samples (spectrum (iv)), and the DL samples $(Mn_{0.3}Ge_9)_{30}$ grown at 433 K (v), was found. The only notable exception was the prominent peak at 6579 eV (F), which was not properly reproduced by the calculations.

As already discussed in the present section, an attempt to recover the missing resonance (F) at 6579 eV with Mn–Mn scattering of near-neighbor impurities in the substitutional model, or in general with the number of Mn absorbers per volume, was not successful. The reason was again the short range order sensitivity of the XANES spectroscopy.

A more realistic possibility was represented by the in-plane uniaxial compressive strain induced by the growth on the oriented Ge(001) substrate. In this latter case, we reported in figure 8(a) the calculation of the unstrained substitutional Mn XAS case, while in (b) and (c) the spectra including an in-plane compressive strain giving rise to an elastic elongation along the normal to the sample. Such an elongation amounted respectively to 4 and 12% and corresponded to a [100] interplanar distance z change from 1.415 to 1.50 Å and to 1.60 Å (see the sketch in figure 8). As a result, the first Ge neighbor distance reached the value of 2.56 Å, while the coordination angle $\mathrm{Ge\hat{M}nGe}$ was reduced to 102° from the nominal value of 109°. One main consequence in the XAS spectra was that the peak at 6579 eV was clearly enhanced because of this large local strain.

Though a precise determination of the structure in case of elastic stress would require the knowledge of values of the elastic constants [34], we observed that the Mn–Ge distance did not change regardless of the Mn concentration. Our intent here was to give a first order rough estimate of the local strain as supported by the EXAFS determination of the first Mn–Ge distance close to 2.50 Å (see section 4). Such a lattice parameter change would be difficult to obtain by XRD because of the very local character of the deformation.

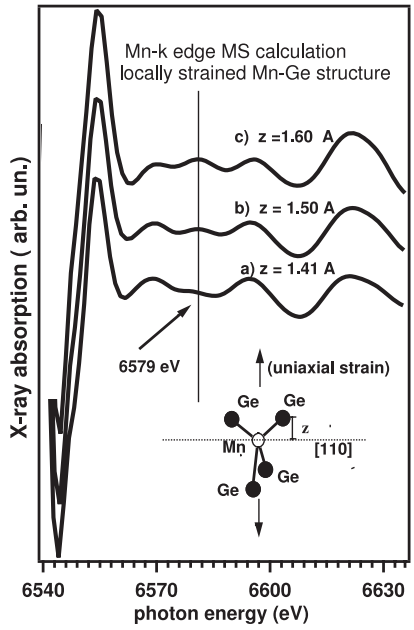

Figure 8. MS XAS calculations of the substitutional Mn model at the Mn K edge. Here the first coordination shell is uniaxially stressed compressively, as shown in the inset. Calculations are reported for different strain values: 0, 5 and 12% for (a), (b) and (c), respectively.

We summarize here the results obtained in the section dedicated to the XANES of the Mn K-edge spectra of Mn in Ge films: (1) at temperatures higher than 343 K, samples grown by MBE were mainly composed by Mn_5Ge_3 alloy; (2) RT implanted subsequently annealed or low temperature ($\leqslant$343 K) MBE samples showed a remarkable content of interstitial T sites; (3) samples implanted at LN or MBE DL alloys at the temperature of 433 K are candidates for the Mn occupation of S sites with good efficiency, showing a sizable degree (a few per cent) of compressive strain.

4. EXAFS analysis

The EXAFS analysis was performed by means of the multiple scattering *ab initio* GnXAS package [35]. Theoretical signals from atomic shells surrounding the Mn absorber were considered to describe the experimental modulation absorption coefficient.

The present alloys, with sizable structural and compositional disorder, showed negligible EXAFS signals from long distance shells and only a few contributions from closer shells were included.

In particular, the occurrence of precipitation of Mn_5Ge_3 crystallites was investigated by monitoring the bond length region between 2.0 and 3.8 Å around the Mn impurity. In such

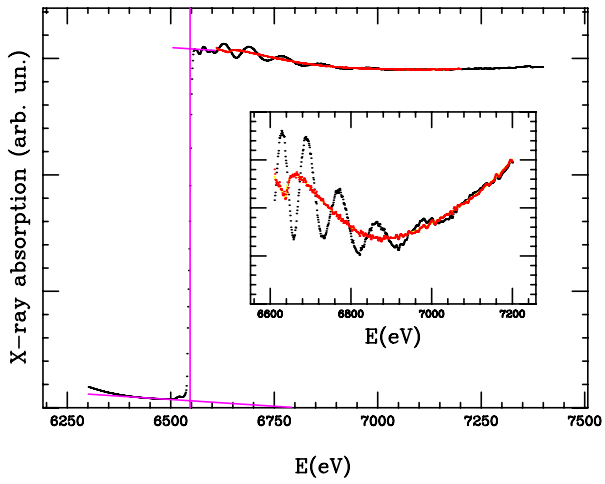

Figure 9. Extraction procedure of EXAFS signal from the Mn K-edge x-ray absorption data of the implanted sample at 80 K with UHV annealing at 673 K. In the inset the presence of a multiple excitation (1s $\rightarrow \epsilon$p, 3s $\rightarrow \epsilon$s) is clearly shown.

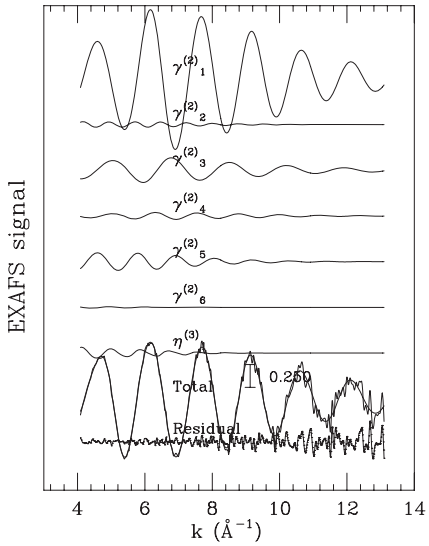

Figure 10. Mn K-edge EXAFS signals related to the implanted sample at 80 K with UHV annealing at 673 K. Here six two-body signals (γ) and one three-body signal (η) are shown.

a range the possibilities of substitutional (S), interstitial (both in the H or T coordination) and alloy (A) occupation sites were represented by particular shell distances. In table 1 the nearest and next nearest neighbor distances of the Mn atomic site for the three cases of Mn site occupation (S, H and T) are reported, while in table 2 the mean distances and occupation numbers for the case of two independent Mn sites in the Mn_5Ge_3 can be found.

Taking into consideration the oxide compound formation and general additional contributions to those of tables 1 and 2, no further improvement was obtained in the fitting of the experimental curves.

The fitting program compared the experimental absorption spectrum $\alpha(E)$ with a modelized one $\alpha_m(E)$. The EXAFS model was composed by the background part and the structural signal $\chi_m(k)$, where the k were the photoelectron wavevectors. The background was given by an atomic absorption $\alpha_0(E)$, a post-edge background function $\alpha_{bkg}(E)$ and possible contributions from additional edges $\alpha_{exc}(E)$ due to many-electron excitations [36]. The resulting theoretical signal was $\alpha_m(E) = \alpha_{bkg}(E) + \alpha_{exc}(E) + \alpha_0(E)\chi_m(E)$.

A hydrogen-like absorption function as the atomic contribution ($\alpha_0(E)$) was used to normalize the EXAFS oscillations filtered from the post-edge background.

During the analysis, the K-edge core ionization potential E_0 was kept fixed at 6542.0 eV while the amplitude reduction factor, S_0^2, ranged around the value of 0.80. A smooth and monotonic background from two third order spline functions was obtained by adding a double electron excitation related to a KM shake-off (1s $\rightarrow \epsilon$p, 3s $\rightarrow \epsilon$s at about 6637 eV). Such a double electron excitation was located about 95 eV above the edge, close to the Fe 3s ionization energy (92 eV), as expected on the basis of the $Z + 1$ rule in x-ray absorption (see figure 9).

Both the possibility of interstitial occupation (in H or T coordination) and of alloy formation were represented by particular shell distances. In particular, the interstitial T short range region was different from that of the pure substitutional because of a strong scattering shell (six Ge atoms) at 2.82 Å. Furthermore, a full occupation of the T sites would correspond to a 4:6 ratio of the first to second shell occupation numbers. An interstitial Mn in the H site would have respectively six and eight Ge atoms at 2.35 Å and 3.66 Å respectively. Finally, an atomic shell at 4.7 Å with 12 Ge atoms was present in both cases of S and T interstitial occupation.

From the above considerations, seven combinations of EXAFS signals were used to represent the data, namely six two-body γ and one three-body η signals to describe the short range order around a single Mn atom [37]. In figure 10 the result of the fit is shown for the particular case of the post-growth annealed LN implanted sample. From the top to the bottom we report six two-body signals (γ) as follows: Ge at 2.45 Å (γ_1); Ge at 4.68 Å (γ_2); Ge at 2.34 Å (γ_3) for a Mn hexagonal occupation; Ge at 3.6 Å (γ_6); Ge at 2.82 Å (γ_4) for tetrahedral interstitial Mn; Mn at 3.06 Å (γ_5) for Mn_5Ge_3 alloy. A single three-body signal (η_1) was used to describe the triangle Mn–Ge–Ge with the two Ge atoms at 2.45 Å and an angle of about 109° between them. The latter signal included the most important among the multiple scattering contributions and a long bond scattering from the shell of 12 Ge atoms at 4.0 Å. In the interstitial T case it was difficult to resolve the scattering from the shell at 2.82 Å from that of the Mn–Mn distance in the Mn_5Ge_3 alloy (an average of eight Mn atoms at 3.04 Å) [32]. It was nevertheless observed that splitting of the Mn–Mn signal in two close shells at such a distance turned out to be crucial to obtain the right value of 8.4 Mn scatterers in the second shell of Mn_5Ge_3. Such a value was usually underestimated when only a single shell distance was used in the multiparametric fit [15].

Using the above procedure we obtained the results reported in table 3 for the main parameters of the signals considered (average atomic distances and their variances).

A controversial aspect of the whole analysis was the value of the nearest neighbor (NN) distance in the substitutional and

Table 3. Average structural parameters (shell distances and variances) obtained by EXAFS for the set of data collected.

		Substitution (S)	Tetrahedral (T)	Alloy (A)
Impl. LN +	R (Å)	2.51(3)		
ann 673 K	σ^2 (Å^2)	0.008(3)		
Impl. RT +	R (Å)	2.53(3)	2.75(3)	
ann 673 K	σ^2 (Å^2)	0.011(3)	0.016(3)	
Impl. 523 K +	R(Å)	2.48(3)	2.82(3)	
ann 673 K	σ^2 (Å^2)	0.011(3)	0.011(3)	
MBE	R (Å)	2.52(3)	2.82(3)	
343 K	σ^2 (Å^2)	0.011(3)	0.029(5)	
MBE	R (Å)	2.50(3)	2.87(3)	3.06(3)
433 K	σ^2 (Å^2)	0.009(3)	0.011(3)	0.003(1)
MBE	R (Å)	2.53(3)	2.81(3)	3.02(4)
523 K	σ^2 (Å^2)	0.006(3)	0.011(3)	0.003(1)
Mn_5Ge_3	R (Å)	2.50(3)	2.83(3)	3.02(4)
	σ^2 (Å^2)	0.006(3)	0.013(3)	0.003(1)
$(Mn_{0.3}Ge_9)_{30}$	R (Å)	2.52(3)		
	σ^2 (Å^2)	0.010(3)		

in the interstitial case, which should also be put in relation to the possible strain effects induced by the substrates, as outlined in section 2.

From the computational point of view, in the local density approximation (LDA) such a Mn NN distance in interstitial T occupation was found to be larger than the Ge–Ge NN distance (2.45 Å) in bulk Ge crystals. In contrast, it was found to be smaller in the case of substitutional Mn atoms [32]. In the present EXAFS analysis we observed an extended Ge–Mn bond length with respect to bulk Ge, in agreement with a similar study about III–V semiconductors [38]. Such discrepancies were not completely unexpected in LDA of small band gap semiconductors and a further improvement in the theoretical approach, possibly including correlation due to the d-state localization of Mn valence electrons, should be considered [39].

In figure 11, the theoretical EXAFS curves compared to the normalized experimental absorption are reported. Such a set of data shows how the amplitude of the $\chi(k)$ oscillations increased with the growth temperature, indicating that the number and/or the configurational order of scatterers around the Mn absorber increased with the temperature. Moreover, a sizable interference between two main signals is observed, while only a single main signal is dominant in samples grown at low temperatures.

In figure 12 the corresponding Fourier transforms of the EXAFS spectra of figure 11 are reported, clearly indicating that the low temperature implanted and the digital alloy samples were intrinsically less affected by strong signals from shells around 3.0 Å when the high temperature formation of the alloy occurred.

Before discussing the resulting EXAFS parameters, we stress that a complete comparison between the two different classes of samples (implanted versus MBE) must take into consideration possible differences in the Mn concentration. We believe that this difference cannot affect our analysis as

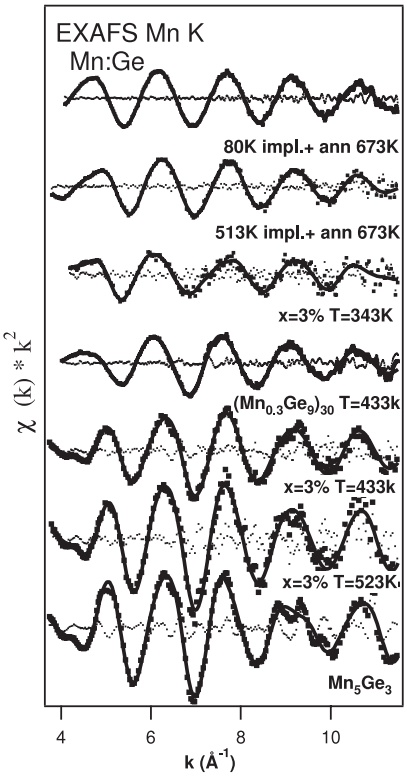

Figure 11. Comparison between theoretical and experimental EXAFS $\chi(k)$ functions for the selected set of samples which best represents the relevant effects observed in Mn_xGe_{1-x} MBE and implanted alloys of the present study.

the Mn distribution in the implanted samples is very well centered around the value of $x = 4 \pm 1\%$. To support this view we also found that EXAFS data were more influenced by the temperature and by the growth process than by the Mn concentration, showing also at very low concentrations the same EXAFS signatures of precipitation as more concentrated samples at similar growth temperatures.

The results of the EXAFS data analysis are reported in table 3 and for the occupation numbers in the form of a diagram in figure 13. An important check of the method used was that the number of Ge neighbors surrounding the Mn impurity was always found to be close to the value of 4 (within 10% of indetermination).

In panel (a) of figure 13 the occupation of the alloy (A) site (N_A) was reported to rapidly increase in the case of MBE samples, while the hexagonal contribution (N_H) (panel (b)) to the interstitial site appeared to be negligible within the error of the determination compared to its nominal value ($N_H = 6$). A clear combination of A and T sites was seen to occur at higher temperature growth by looking at panel (c).

The latter observation barred the occurrence of the simultaneous occupation of the interstitial T and H sites, with their characteristic distance of 3.06 Å, from explaining the frequent EXAFS observation of the main alloy Mn–Mn distance (see figure 6) detected also at low Mn (less than 3%) concentration.

Indeed, in the MBE growth samples and to a lower extent in implanted samples, the content of alloy component

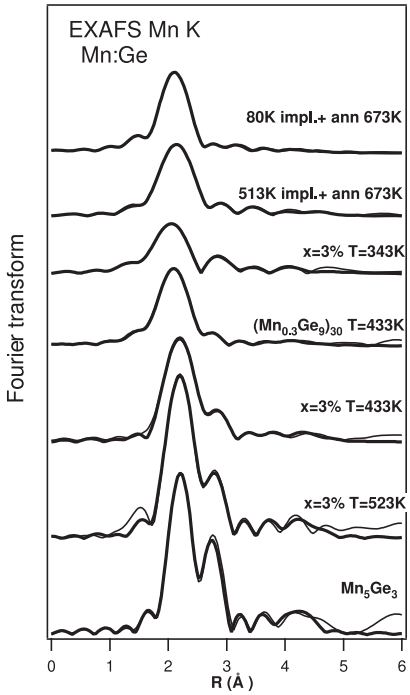

Figure 12. Comparison between theoretical and experimental Fourier transform of EXAFS $\chi(k)$ functions for the selected set of samples which best represents the behavior of Mn_xGe_{1-x} MBE and implanted samples.

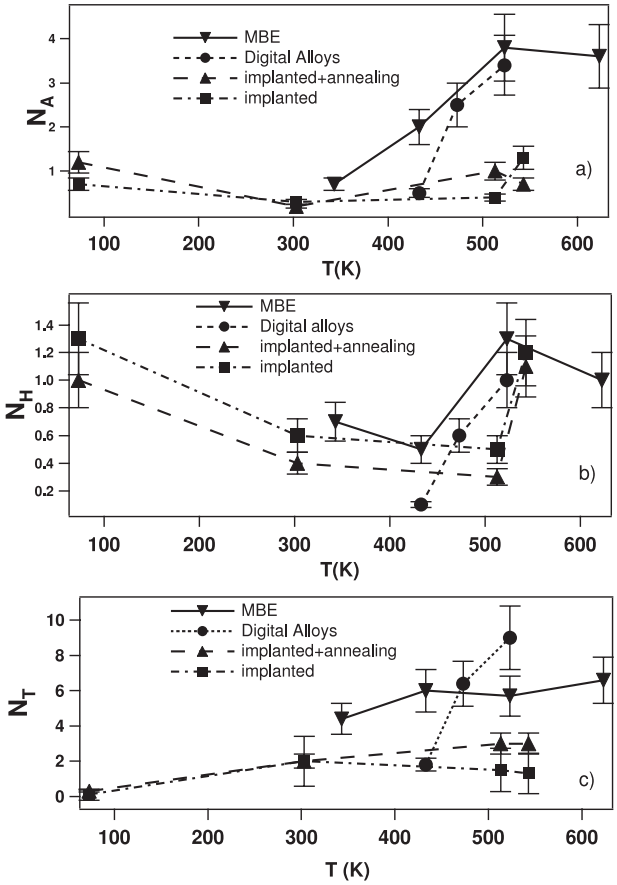

Figure 13. Summary of shell occupation numbers obtained by EXAFS. From (a) to (c) we observe the occupation numbers of the alloy (N_A), the interstitial hexagonal (N_H) Mn and the interstitial tetrahedral (N_T) Mn.

(N_A in panel (a)) was accompanied by a corresponding presence of interstitial tetrahedral site occupation (N_T) (panel (c)) independently of the growth temperature. By reducing the growth temperature in MBE samples only N_A is reduced with respect to N_T. In the case of implanted samples both the occupation numbers N_A and N_T remained well below 30% of the nominal value, indicating the formation of an almost pure substitutional occupation, but with some degree of disorder, as observed from the EXAFS signal. In particular, the implanted sample at 80 K showed remarkable single phase and thermal stability.

A possible interpretation of these data is that tetrahedral interstitial occupation is the precursor phase of the alloy and the failure in occupation of such interstitial sites hindered the alloy formation. MBE samples grown at 343 K did not turn completely to alloy and showed mostly Mn in tetrahedral interstitial sites.

A second relevant case is given by the MBE DL alloy samples $(Mn_{0.3}Ge_9)_{30}$ grown at 433 K. In this case the EXAFS analysis showed the least amount of alloy ($N_A = 1.2$), amounting to about one-fourth of the contribution found in the MBE samples at the same temperature, and a negligible tetrahedral interstitial site occupation. From this evidence we can estimate that the DL alloys did not simply raise the temperature threshold for the alloy transformation but raised a potential barrier against the interstitial tetrahedral occupation. DL alloys are clearly metastable structures, as can be observed from the abrupt change in phase composition as the growth temperature is slightly increased to $T > 433$ K [40].

It must be noted that clusters of neighboring substitutional and interstitial sites have been demonstrated to be more stable than clusters of pure substitutional sites in the case of Mn in GaAs [41]. Moreover, the experimental data presented here, and in particular the fact that the alloy formation began from the occupation of interstitial sites, were supported by the observations presented in [23]. In that study one of the tetrahedra composing the Ge_3Mn_5 structure was identified as being the building block of the GeMn nanocolumnar structures. It can be shown that the base of this tetrahedron, containing distances Ge–Mn = 2.50 and Mn–Mn = 2.80, can be reproduced in the Ge structure by occupying a T site (center of the cube) and an S site (center of a face) with Mn atoms. The aim of the future studies should point towards the preparation procedures of single phase samples in order to provide major insights into the transformation process at the basis of this long-standing problem.

5. Conclusions

In conclusion, by means of a complete XAS investigation of MnGe alloys at low Mn concentrations and two different growth techniques, we have singled out the Mn atom occupation site during various phases of the incorporation at various temperatures by MBE or implantation growth techniques. Although in the Ge unit cell the distance between

the hexagonal and the interstitial site (see figure 6) is exactly 3.05 Å, the same as the Mn–Mn distance in the Mn_5Ge_3 alloy, we excluded that such a preliminary configuration was the precursor of the alloy. All the indications found here showed that, especially in the case of MBE growth, the formation of Mn_5Ge_3 phase detected by EXAFS was probably promoted by the occupation of interstitial tetrahedral sites. Such a finding was in agreement with the observations of Rovezzi *et al* [23] on nanocolumns of GeMn in Ge and with the results obtained for the III–V DMSs [33, 21].

At the basis of this observation is the well known stability of the tetrahedral site with respect to the hexagonal interstitial site and in general the preference of Mn atoms to occupy interstitial sites if compared to other TM atoms [42].

Furthermore, from both EXAFS and XANES analysis we came to the conclusion that the digital alloys or low temperature implantation are reasonably free from alloying processes and interstitial site occupation. Finally, a sizable compressive strain was detected in the most stable films with substitutional incorporation of Mn.

Acknowledgments

G Robouch and A Marcelli (LNF-INFN Frascati (Italy)) are gratefully acknowledged for fruitful discussions. GILDA is a project jointly financed by CNR and INFN.

References

[1] Park Y D, Hanbicki A T, Erwin S C, Hellberg C S, Sullivan J M, Mattson J E, Ambrose T F, Wilson A, Spanos G and Jonker B T 2002 *Science* **295** 651
[2] Ohno Y, Young D K, Beschoten B, Matsukura F, Ohno H and Awschalom D D 1999 *Nature* **402** 790
[3] Madelung O (ed) 1996 *Semiconductors-Basic Data* (Berlin: Springer)
[4] Cho S, Choi S, Hong S C, Kim Y, Ketterson J B, Kim B-J, Kim Y C and Jung J-H 2002 *Phys. Rev.* B **66** 033303
[5] Kang J-S *et al* 2005 *Phys. Rev. Lett.* **94** 147202
[6] Li A P, Shen J, Thompson J R and Weitering H H 2005 *Appl. Phys. Lett.* **86** 152507
[7] Zeng C, Zhang Z, van Benthem K, Chrisholm M F and Weitering H H 2008 *Phys. Rev. Lett.* **100** 066101
[8] Goswami R, Kioseoglou G, Hanbicki A T, van't Erve O M J, Jonker B T and Spanos G 2005 *Appl. Phys. Lett.* **86** 032509
[9] Ayoub J-P, Favre L, Berbezier I, Ronda A, Morresi L and Pinto N 2007 *Appl. Phys. Lett.* **91** 141920
[10] Pinto N, Morresi L, Ficcadenti M, Murri R, D'Orazio F, Lucari F, Boarino L and Amato G 2005 *Phys. Rev.* B **72** 165203
[11] Nazmul A M, Ameniya T, Shuto Y, Sugahara S and Tanaka M 2005 *Phys. Rev. Lett.* **95** 017201
[12] Liu L, Chen N, Yin Z, Yang F, Zhou J and Zhang F 2004 *J. Cryst. Growth* **273** 106
[13] Picozzi S, Ottaviano L, Passacantando M, Profeta G, Continenza A, Priolo F, Kim M and Freeman A J 2005 *Appl. Phys. Lett.* **86** 062501
[14] Ottaviano L, Passacantando M, Picozzi S, Continenza A, Gunnella R, Verna A, Bihlmayer G, Impellizzeri G and Priolo F 2006 *Appl. Phys. Lett.* **88** 061907
[15] Ottaviano L, Passacantando M, Verna A, Gunnella R, Principi E, Di Cicco A, Impellizzeri G and Priolo F 2006 *J. Appl. Phys.* **100** 063528
[16] Passacantando M, Ottaviano L, D'Orazio F, Lucari F, De Biase M, Impellizzeri G and Priolo F 2006 *Phys. Rev.* B **73** 195207
[17] Verna A *et al* 2006 *Phys. Rev.* B **74** 085204
[18] Ottaviano L, Verna A, Grossi V, Parisse P, Piperno S, Passacantando M, Impellizzeri G and Priolo F 2007 *Surf. Sci.* **601** 2623
[19] Ottaviano L, Continenza A, Profeta G, Impellizzeri G, Irrera A, Kazakova O and Gunnella R 2010 submitted
[20] Soo Y L, Kioseoglu G, Chen X, Luo H, Kao Y H, Sasaki Y, Lui X and Furdyna J K 2002 *Appl. Phys. Lett.* **80** 2654
Soo Y L *et al* 2003 *Appl. Phys. Lett.* **83** 2354
[21] d'Acapito F, Smolentsev G, Boscherini F, Piccin M, Bais G, Rubini S, Martelli F and Franciosi A 2006 *Phys. Rev.* B **73** 035314
[22] Wolska A, Lawniczak-Jablonska K, Klepka M, Wlaczak M S and Misiuk A 2007 *Phys. Rev.* B **75** 113201
[23] Rovezzi M, Devillers T, Arras E, D'Acapito F, Barski A, Jamet M and Pochet P 2008 *Appl. Phys. Lett.* **92** 242510
[24] Norton D P, Pearton S J, Hebard A F, Theodoropoulou N, Boatner L A and Wilson R G 2003 *Appl. Phys. Lett.* **82** 239
[25] D'Orazio F, Lucari F, Santucci S, Picozzi P, Verna A, Passacantando M, Pinto N, Morresi L, Gunnella R and Murri R 2003 *J. Magn. Magn. Mater.* **262** 158
[26] Pinto N, Morresi L, Gunnella R, Murri R, D'Orazio F, Lucari F, Santucci S, Picozzi P, Passacantando M and Verna A 2003 *J. Mater. Sci., Mater. Electron.* **14** 337
[27] Gunnella R, Morresi L, Pinto N, Murri R, Ottaviano L, Passacantando M, D'Orazio F and Lucari F 2005 *Surf. Sci.* **577** 22
[28] d'Acapito F *et al* 1998 *ESRF Newslett.* **30** 42
[29] Pascarelli S, Boscherini F, d'Acapito F, Hrdy J, Meneghini C and Mobilio S 1996 *J. Synchrotron Radiat.* **3** 147
[30] Ottaviano L, Passacantando M, Verna A, D'Amico F and Gunnella R 2007 *Appl. Phys. Lett.* **90** 242105
[31] Sebilleau D, Gunnella R, Di Matteo S, Wu Z-Y and Natoli C R 2006 *J. Phys.: Condens. Matter* **18** R175–230 and references therein
[32] Continenza A, Profeta G and Picozzi S 2006 *Phys. Rev.* B **73** 035212
[33] Yu K M, Walukiewicz W, Wojtowics T, Kuryliszyn I, Liu X, Sasaki Y and Furdyna J K 2002 *Phys. Rev.* B **65** 201303
[34] d'Acapito F 2004 *J. Appl. Phys.* **96** 369
[35] Filipponi A and Di Cicco A 1995 *Phys. Rev.* B **52** 15135
[36] Di Cicco A 1996 *Phys. Rev.* B **53** 6174
[37] Filipponi A, Di Cicco A and Natoli C R 1995 *Phys. Rev.* B **52** 15122 1996
[38] Bacewicz R, Twarog A, Malinowska A, Wojtowicz T, Liu X and Furdyna J K 2005 *J. Phys. Chem. Solids* **66** 2004
[39] Rovezzi M, D'Acapito F, Navarro-Quezada A, Faina B, Li T, Bonanni A, Filippone F, Amore Bonapasta A and Dietl T 2009 *Phys. Rev.* B **79** 195209
[40] Gunnella R, Pinto N, Morresi L, Abbas M and Di Cicco A 2008 *J. Non-Cryst. Solids* **354** 4193
[41] Mahadevan P and Zunger A 2003 *Phys. Rev.* B **68** 075202
[42] Continenza A, Profeta G and Picozzi S 2006 *Appl. Phys. Lett.* **89** 202510